

See discussions, stats, and author profiles for this publication at: <https://www.researchgate.net/publication/265964978>

Differential sputtering correction for ion microscopy with image depth profile

ARTICLE *in* ANALYTICAL CHEMISTRY · JANUARY 1982

Impact Factor: 5.64

CITATIONS

2

READS

20

3 AUTHORS, INCLUDING:



[Adam Patkin](#)

PerkinElmer

4 PUBLICATIONS 67 CITATIONS

[SEE PROFILE](#)



[Subhash Chandra](#)

Cornell University

78 PUBLICATIONS 1,687 CITATIONS

[SEE PROFILE](#)

dependence of CrSc-1 site intensity. However, the signal to noise ratios obtained were not large enough to effectively compete with the previously developed method involving scandium and erbium doped calcium fluoride precipitates (7). Nonetheless, observation of the CrSc-1 site was significant since it showed that mixed clusters could be efficiently formed in magnesium oxide as well.

Double doped precipitates of Al^{3+} , Rh^{3+} , and Fe^{3+} plus Cr^{3+} were studied to see if new sites were formed. Although no new sites were unambiguously identified, it is possible that chromium in Cr-Rh clusters does fluoresce from the 2E_g level at the same wavelength as the C site. In this case, a quantitative determination of rhodium would be impossible due to overlap with the higher intensity fluorescence from Cr-Cr clusters. No new sites were observed in precipitates containing iron or aluminum. Iron may quench chromium fluorescence from mixed clusters, while aluminum may be too small to cluster efficiently. Clusters of chromium with tetravalent ions were searched for in double doped precipitates containing Zr^{4+} , Ir^{3+} , Os^{4+} , and Ru^{3+} . (Upon ignition in air, iridium and ruthenium are oxidized.) No new lines or spectral changes were observed. Iridium, osmium, and ruthenium could have low lying levels which might quench chromium fluorescence, but zirconium(IV), a closed shell configuration ion, has none.

New lines are observed in chromium doped magnesium oxide containing lithium and sodium (Figure 4c,d). Although nominally referred to as the CrLi-1 and CrNa-1 sites in Table I, conclusive identification of these sites as chromium-monovalent ion clusters is not possible, especially in light of the promotional effect that these ions have on the D site intensities. Nonetheless, these lines are observed only when the respective monovalent ions are present. Pilla et al. (17) have identified lines in $\text{MgO}:\text{Cr}^{3+}$ single crystals which they

interpreted as arising from chromium defect aggregates containing sodium and potassium. Neither of these lines were unambiguously identified in the appropriate monovalent ion doped precipitates. Even if the lines observed here were to be connected to clusters of chromium with lithium or sodium, their use in chemical determinations would be limited due to low signal to noise ratios at relatively high concentrations.

LITERATURE CITED

- (1) Gustafson, F. J.; Wright, J. C. *Anal. Chem.* **1977**, *49*, 1680.
- (2) Wright, J. C.; Gustafson, F. J. *Anal. Chem.* **1978**, *50*, 1147A.
- (3) Gustafson, F. J.; Wright, J. C. *Anal. Chem.* **1979**, *51*, 1762.
- (4) Johnston, M. V.; Wright, J. C. *Anal. Chem.* **1979**, *51*, 1774.
- (5) Wright, J. C. "Modern Fluorescence Spectroscopy"; Wehry, E. L., Ed.; Plenum Press: New York, 1981; Vol. 4.
- (6) Johnston, M. V.; Wright, J. C. *Anal. Chem.* **1981**, *53*, 1050.
- (7) Johnston, M. V.; Wright, J. C. *Anal. Chem.* **1981**, *53*, 1054.
- (8) Wright, J. C. *Anal. Chem.* **1977**, *49*, 1690.
- (9) Wertz, J. E.; Auzins, P. *Phys. Rev.* **1957**, *106*, 484.
- (10) Henderson, B.; Wertz, J. E. *Adv. Phys.* **1968**, *17*, 749.
- (11) Griffiths, J. E. E.; Orton, J. W. *Proc. Phys. Soc. London* **1959**, *73*, 948.
- (12) Yager, T. A.; Kingery, W. D. *Rev. Sci. Instrum.* **1980**, *51*, 464.
- (13) Schawlow, A. L. *J. Appl. Phys.* **1962**, *33*, 395.
- (14) Imbusch, G. F.; Schawlow, A. L.; May, A. D.; Sugano, S. *Phys. Rev.* **1965**, *140*, A830.
- (15) Henry, M. O.; Larkin, J. P.; Imbusch, G. F. *Phys. Rev. B* **1976**, *13*, 1893.
- (16) Boyrivent, A.; Duval, E.; Montagna, M.; Villani, G.; Pilla, O. J. *Phys. C* **1979**, *12*, L803.
- (17) Pilla, O.; Montagna, M.; Villani, G.; Santucci, S. *Phys. Rev. B* **1980**, *21*, 4859.
- (18) Miller, M. P.; Tallant, D. R.; Gustafson, F. J.; Wright, J. C. *Anal. Chem.* **1977**, *49*, 1474.
- (19) Tanabe, Y.; Sugano, S. *J. Phys. Soc. Jpn.* **1954**, *753*, 766.
- (20) Glass, A. M. *J. Chem. Phys.* **1967**, *46*, 2080.

RECEIVED for review May 5, 1982. Accepted September 19, 1982. We wish to acknowledge the National Science Foundation for the support of this research under Grants CHE7825306 and CHE8119893.

Differential Sputtering Correction for Ion Microscopy with Image Depth Profiling

Adam J. Patkin, Subhash Chandra, and George H. Morrison*

Department of Chemistry, Baker Laboratory of Chemistry, Cornell University, Ithaca, New York 14853

A first-order correction for differential sputtering is made to ion micrographs using image depth profiling. This is done by first recording the ion image to be corrected and then sputtering down to the substrate while recording a series of images at the substrate's mass. A time-domain "burn-through" map showing the time each location of the sample first sputters through to the substrate is then generated. This map is used to make a linear correction for differential sputtering induced ion intensity artifacts to the initial sample images. $^{40}\text{Ca}^+$ ion images of a radish root tip stele cell region on a tantalum substrate are corrected in this fashion. Relative sputtering rates of 1.5 and 1.2 compared to the cytoplasm were found for the cell walls and nuclei, respectively.

Ion microscopy, a form of secondary ion mass spectrometry (SIMS), is an analytical technique with the ability to generate mass-resolved images of a solid sample with elemental detection limits at the parts per million level (1). A 2-20-keV

primary ion beam is used to sputter the top atomic layers of the sample, and secondary ions emitted from this region are extracted and mass analyzed to produce ion images. Qualitative interpretations of ion images have been shown to be useful in studies of elemental distributions in biological tissues (2-8). However, quantitative interpretations of ion images can be erroneous because of the problem of differential sputtering, a phenomenon first pointed out by Galle (9) and more recently by Farmer et al. (10).

The observed SIMS secondary ion intensity may be described by the equation of Morrison and Slodzian (1)

$$I = \tau C_m S i_p a_0 \quad (1)$$

where I is the measured secondary ion current, τ the practical ion yield, C_m the atomic concentration of the element M (corrected for its isotopic abundance), S the total sputtering yield (number of atoms of any kind removed per incoming particle), i_p the number of primary particles arriving per unit time and unit area on the target surface, and a_0 is the analyzed area on the target surface.

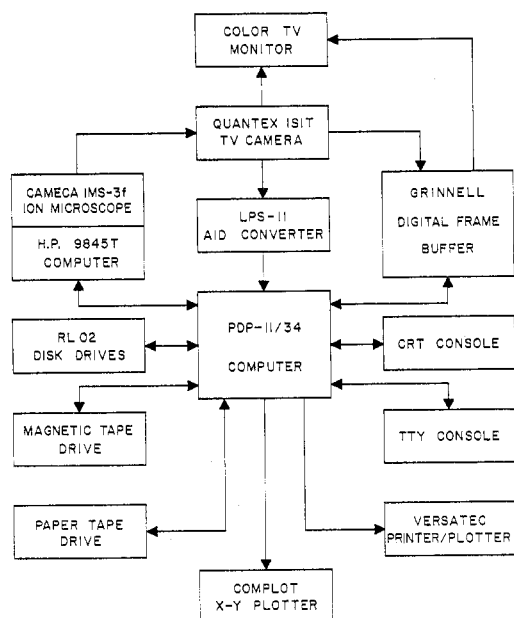


Figure 1. System configuration.

Local variations in composition across a spatially heterogeneous sample's surface cause different regions of the sample to sputter at different rates. Since the observed intensity I is proportional to S , this causes erroneous ion intensity enhancements, and therefore higher apparent elemental concentrations, for the more rapidly sputtered regions. Biological tissue is a very heterogeneous material, and is thus particularly prone to differential sputtering. An appropriate correction for differential sputtering is therefore needed for any type of quantitative work for biological tissue in particular, and spatially heterogeneous materials in general.

This paper demonstrates a first-order differential sputtering correction by use of digital image processing. It is performed by mounting a thin biological sample upon a substrate which produces secondary ions at a mass not observed in the sample. Images at masses of interest are recorded from the sample. The sample is then sputtered down to the substrate while a series of ion images is recorded, with increasing depth, at the substrate's mass by the image depth profiling (IDP) method of Patkin and Morrison (11). A "burn-through" map is generated from the IDP images, recording the time each location of the sample sputtered down to the substrate. This time-domain burn-through map is then used to correct the initial sample ion images for differential sputtering induced ion intensity artifacts.

EXPERIMENTAL SECTION

Instrumentation. Ion images were obtained with a CAMECA IMS-3f ion microscope. This ion microscope obtains images at selected mass/charge ratios which retain the original spatial relationships of the elements in the sample (12).

The microscopic image digital acquisition system (MIDAS) (13) shown in Figure 1 was used to record images. MIDAS consists of a low-light level ISIT (intensified silicon intensified target) TV camera, digital frame buffer (digitally stores a $256 \times 240 \times 12$ -bit image), analog/digital converter, computer, graphics display screen, and associated computer software. The TV camera is focused upon the fluorescent screen of the ion microscope. The images are acquired by the TV camera/frame buffer and stored by the computer. Changes from the original MIDAS description (13) include replacement of the CAMECA IMS-300 ion microscope with a more sophisticated CAMECA IMS-3f and dedicated H.P. 9845T microcomputer, replacement of the DEC PDP-11/20 minicomputer and GT-40 graphics display terminal with a DEC PDP-11/34A with 256K byte RAM and two 10M byte disks, and the use of a $f/2.0$, 102-mm zoom lens on the TV camera set at 40 mm for a 50- μ m field-of-view.

Chart I

$$I_{x,y}^m = \begin{cases} 0 & \text{current value} & 0 & \text{next value} \\ 0 & >0 & 0 \\ T & 0 & >0 \\ \text{current value} & >0 & >0 \end{cases}$$

Computer Software. Programs were written in FORTRAN IV, RATFOR (a structured FORTRAN IV preprocessor), and MACRO-11 assembly language.

There are four stages for differential sputtering correction by image depth profiling and digital image processing: acquisition of the image data, amendment of the data for detector and SIMS induced artifacts, image display, and the calculation of the relative differential sputtering rates of various sample features. Five separate but related programs were used for these functions.

IMAGE performs TV image acquisition, disk input/output of images, image display, and registration.

GRFTDK acquires a series of images and transfers them to disk storage at an operator defined rate of up to one image every 8 s.

DETCOR corrects images for spatial inhomogeneities in the image detector system. This is performed by acquiring a standard image of a smooth Si (100) single crystal, with the IMS-3f immersion lens optics slightly defocused to provide a uniformly intense ion image. The MIDAS output image is influenced by nonuniform detector response and degradation so that it appears inhomogeneous. DETCOR determines the correction factor at each pixel necessary to bring that pixel's intensity up to the maximum intensity of the standard image, correcting for detector system heterogeneity. It then uses this factor to correct the current elemental image.

GCONV converts raw image intensities to the corresponding ion intensity by using an empirically derived calibration equation.

DISCOR generates the burn-through map and then uses it to correct the image for differential sputtering. This is done by initially setting each pixel of the map to zero. The substrate images acquired by GRFTDK are then sequentially analyzed and the burn-through map updated as shown in Chart I, where $I_{x,y}^m$ is the new value of the pixel located at x,y in the burn-through map, current value is the value currently stored in that location of the burn-through map and next value is the intensity at location x,y of the image currently being examined in the GRFTDK depth profile sequence. T is the sputtering time at which the GRFTDK image being examined was acquired.

Simply, this functions as follows: Since the substrate on which the sample is mounted is being imaged, any pixel with a nonzero intensity indicates the sample has been completely sputtered away at that location. To avoid spurious readings, however, the program waits until a location gives a continuous series of nonzero substrate ion intensities in the IDP sequence before assigning that location a burn-through time. The burn-through time assigned is the time at which the first of these images was acquired. This procedure is repeated for every image in the IDP sequence, ultimately yielding the burn-through map which contains the time at which each pixel first sputtered through to the substrate.

At this point the burn-through map is used to perform a linear correction to the observed image intensities of the elements of interest in the sample such that

$$I_{x,y}^c = I_{x,y}^f \frac{\text{burn-through time}}{\text{total sputtering time}}$$

where I^c is the differential sputtering corrected image and I^f is the detector discrimination corrected and ion intensity converted elemental image. This gives an ion image corrected, at least to a first approximation, for differential sputtering effects. This correction is based on two assumptions. The first is that the observed secondary ion intensity is proportional to the sputter rate. The second assumption requires that a given region of the sample sputters at a uniform rate throughout the course of the analysis.

Analytical Procedure. The IMS-3f instrumental conditions are shown in Table I. The parameters were chosen to optimize

Table I. Instrumental Operating Conditions

primary ions	Ar ⁺ , O ₂ ⁺
primary ion energy	10 keV
primary ion current	3.6×10^{-4} A/cm ²
sputtered area of sample	5.6×10^{-5} cm ²
secondary ion polarity	positive
transfer optics	150 μ m
vacuum at sample	3×10^{-8} torr
image field-of-view	50 μ m
image integration period	2 s
time between images	8–40 s

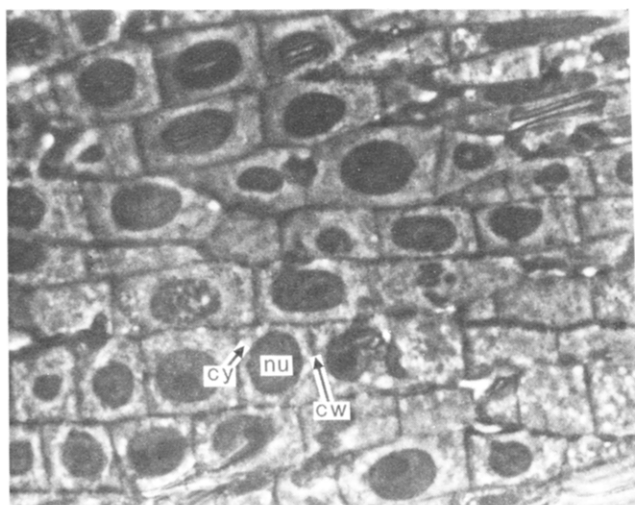


Figure 2. Light micrograph of radish root tip stele cell region (nu = nucleus, cw = cell wall, cy = cytoplasm).

image quality, intensity, and sample sputtering rate. The time between images was chosen on the basis of the primary ion beam species and sample thickness.

Sample Preparation. Root tips of *Raphanus sativus* (radish) seedlings were selected for the study because of their well-defined intracellular calcium distribution. Pieces of root tips 1 to 2 mm in length were chemically fixed for 1 h with 5% glutaraldehyde in 0.03 M Pipes buffer [*N,N'*-bis(2-ethanolsulfonic acid)piperazine] at pH 6.8 (14). Root tips were washed with 0.15 M Pipes buffer and then postfixed for 1 h in 1% osmium tetroxide in the same buffer. After dehydration in ethanol (70–90%) and propylene oxide, the tissue pieces were embedded in low viscosity resin (15). Sections were cut on distilled water using a LKB Ultratome III and transferred onto a polished tantalum disk. Tantalum was selected as a substrate because it was not expected to be present in the tissue. Sections were then stored under vacuum until analyzed in the ion microscope.

RESULTS AND DISCUSSION

Calcium in plant root tip cells was chosen for analysis due to its well-defined intracellular distribution (16). A light micrograph of the stele cell region of a radish root tip section is shown in Figure 2. Figure 3 is a $^{40}\text{Ca}^+$ ion micrograph clearly showing higher intensity of calcium in nuclei and cell walls than in cytoplasm. The severity of differential sputtering is indicated by Figure 4. This is not an image of $^{40}\text{Ca}^+$ but of the substrate, $^{181}\text{Ta}^+$, taken in the course of the image depth profile. These features clearly show that differential sputtering causes the nuclei and cell walls to sputter away well before the cytoplasm region. This is a serious effect which must be considered in any quantitative work.

Figure 5 is a typical burn-through map, with the lighter areas indicating the locations requiring the longest time to sputter away. The map clearly shows the cell walls as the most rapid sputtering features followed by the nuclei and then the cytoplasm. This root tip section was 0.5 μ m thick and took ~5 min to completely burn through to the substrate.

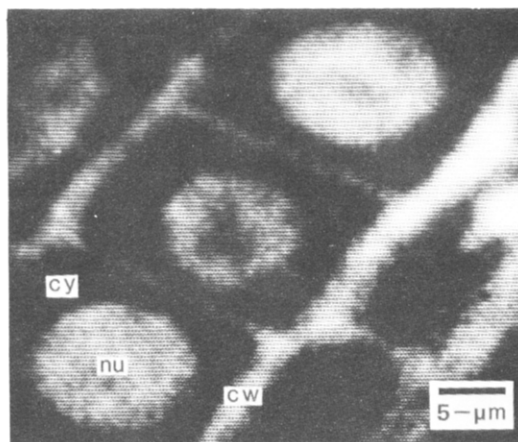


Figure 3. $^{40}\text{Ca}^+$ ion micrograph of stele cells (nu = nucleus, cw = cell wall, cy = cytoplasm).

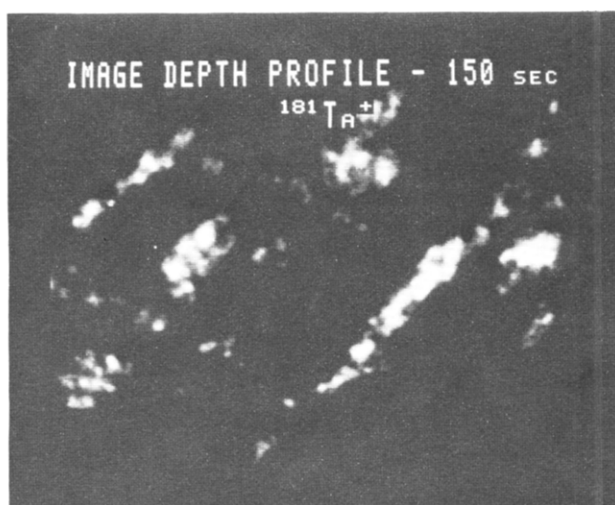


Figure 4. $^{181}\text{Ta}^+$ ion micrograph of substrate 150 s into image depth profile.

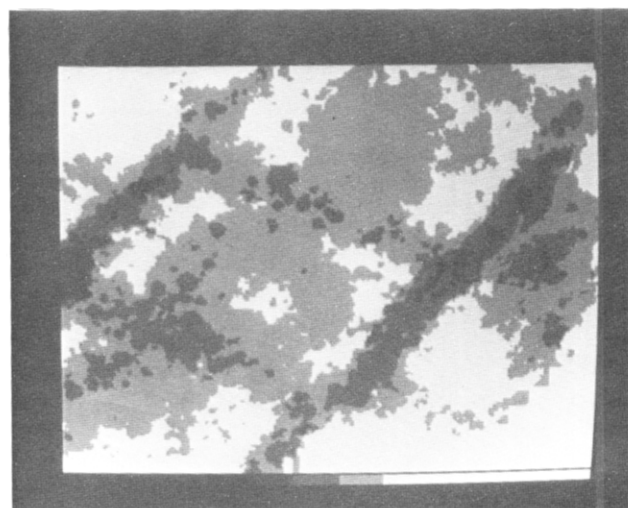


Figure 5. Time-domain burn-through map.

Figure 6 presents the raw $^{40}\text{Ca}^+$ ion image and the same image after detector discrimination, ion intensity conversion, and differential sputtering corrections. Both images have been normalized to the same maximum intensity. Significant differences in the distribution of calcium in the tissue are observed, and the corrected image more accurately indicates the presence of calcium in the respective features, especially in the cytoplasm. This image more closely demonstrates the

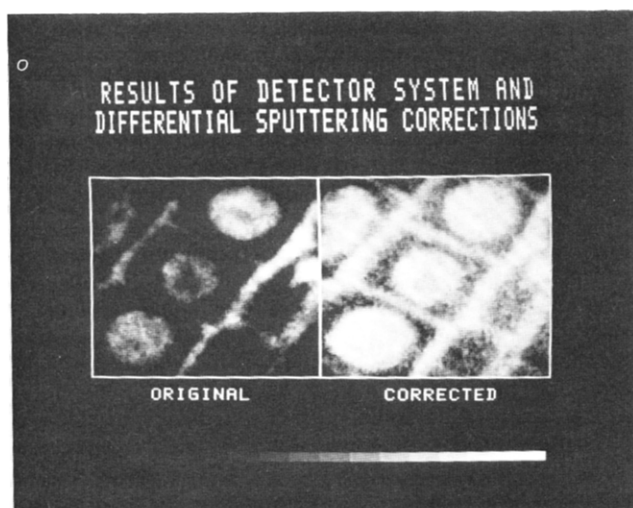


Figure 6. Comparison of original elemental ion image and same image after detector discrimination, ion intensity conversion, and differential sputtering corrections.

Table II. Average R_f Values by Section Thickness

primary beam	cellular feature	R_f values		
		0.25 μ M thick section	0.50 μ M thick section	1.0 μ M thick section
Ar ⁺	R_f cell walls	1.51 \pm 0.22	1.46 \pm 0.04	1.19 \pm 0.06
	R_f nuclei	1.20 \pm 0.04	1.16 \pm 0.02	1.09 \pm 0.06
O ₂ ⁺	R_f cell walls	1.30 \pm 0.08	1.50 \pm 0.02	1.17 \pm 0.01
	R_f nuclei	1.18 \pm 0.13	1.18 \pm 0.04	1.15 \pm 0.01

physiological distribution expected in the in vivo situation. Quantitatively there has been a change in the relative intensities of different features. This will obviously affect the results when converting finally from ion intensity to concentration.

The relative feature sputtering rates R_f can be calculated once the burn-through map has been generated by ratioing the average burn-through times of different features. Table II contains the average R_f values and corresponding standard deviations for cell walls and nuclei in the stele cell region of radish root tip cells under both Ar⁺ and O₂⁺ bombardment. The sputter rates have been normalized to the cytoplasm sputter rate, the slowest sputtering feature.

The R_f values indicate that differential sputtering makes cell walls appear to have 1.5 times and nuclei 1.2 times more calcium (or any other element) than cytoplasm. Like results have been observed in our laboratory with corn and pea root tip cells. Galle (9) has also reported nuclei to sputter faster than cytoplasm in frog nucleated red blood cells. The differentially sputtering nature of biological tissue may be due to its heterogeneous chemical composition. In the case of plant cells, cell wall is primarily composed of polysaccharides (cellulose, hemicellulose, pectine, etc.), while the nucleus is basically a proteinous material rich in DNA (deoxyribonucleic acid), RNA (ribonucleic acid), nucleoproteins, and histone proteins.

A burn-through map at a substrate mass also revealed that epoxy (where tissue is not present) was the last to sputter through (i.e., after cytoplasm). This helps to explain the influence of epoxy in the differential sputtering of epoxy-infiltrated biological tissue. In the case of plants, cell walls are denser material than nuclei and cytoplasm; hence there may be more penetration of epoxy (mass per unit area) into the

less dense cytoplasm than the denser nuclei or still more dense cell walls.

It is interesting to note that both primary beam species induce similar R_f values even though in addition to the differences in reactivity of these two species the average tissue sputter rate for an Ar⁺ primary beam is greater than that observed with O₂⁺ primary beam.

The R_f values indicate the possibility that our assumption of uniform sputter rate with depth may not necessarily be valid, at least when section thickness exceeds 0.5 μ m. The decrease of the R_f value with increasing sample thickness indicates significant sample homogenization. In fact, partial diffusion of ⁴⁰Ca⁺ was observed to occur after several minutes of bombardment, possibly due to local sample heating or charge-induced diffusion. However, the basic sample structure appears unchanged as cellular features are well-defined in the ¹⁸¹Ta⁺ image and burn-through maps.

Factors other than differential sputtering, such as sample surface topology (17) and matrix effects (18), can also influence the observed secondary ion signal intensity, often by several orders of magnitude. Several methods of dealing with these problems have been examined elsewhere (19) and are beyond the scope of this discussion. While the influence of these factors, particularly the matrix effects, may be larger than that of differential sputtering, any comprehensive quantitation procedure will have to include corrections for differential sputtering.

In summary, differential sputtering presents a problem in the quantification of ion images, particularly for biological thin sections where cellular organelles differ widely in their chemical composition. Image depth profiling has been used to make first-order corrections for this problem. This method of correction is useful when a thin flat sample is deposited on a substrate. In addition to biological tissues this technique should also be applicable to other thin films, such as certain types of semiconductor devices and metallurgical samples.

ACKNOWLEDGMENT

The authors wish to acknowledge the help of William C. Harris, Jr., in manuscript preparation.

LITERATURE CITED

- (1) Morrison, G. H.; Slodzian, G. *Anal. Chem.* **1975**, *47*, 932A-943A.
- (2) Spurr, A. K. *Scanning Electron Microsc.* **1980**, *3*, 97-109.
- (3) Frostell, G.; Larsson, S. J.; Lodding, A.; Odellius, H.; Peterson, L. G. *Scand. J. Dent. Res.* **1977**, *85*, 18-21.
- (4) Burns-Bellhorn, M. S.; Lewis, R. K. *Exp. Eye Res.* **1976**, *22*, 505-518.
- (5) Burns-Bellhorn, M. S.; File, B. M. *Anal. Biochem.* **1979**, *92*, 213-221.
- (6) Galle, P. *Ann. Phys. Biol. Med.* **1970**, *4*, 83-94.
- (7) Truchet, M. J. *Microsc. Biol. Cell.* **1975**, *24*, 1-21.
- (8) Campbell, N. A.; Stika, K. M.; Morrison, G. H. *Science* **1979**, *204*, 185-187.
- (9) Galle, P. "Symposium on Microprobe Analysis as Applied to Cells and Tissues", Battelle Research Center, Seattle, WA; Academic Press: London, 1973; 89-105.
- (10) Farmer, M. E.; Linton, R. W.; Ingram, P.; Sommer, J. R.; Shelburne, J. D. *J. Microsc. (Oxford)* **1981**, *124*, RP1-RP2.
- (11) Patkin, A. J.; Morrison, G. H. *Anal. Chem.* **1982**, *54*, 2-5.
- (12) Ruberol, J. M.; Leqpareu, M.; Autier, B.; Gourgout, J. M. VIII International Congress on X-Ray Optics and Microanalyses and the 12th Annual Conference of the Microbeam Analysis Society, Boston, MA, 1977, 133A-133D.
- (13) Furman, B. K.; Morrison, G. H. *Anal. Chem.* **1980**, *52*, 2305-2310.
- (14) Salema, R.; Brandao, I. J. *Submicrosc. Cytol.* **1973**, *5*, 79-96.
- (15) Spurr, A. R. *J. Ultrastruct. Res.* **1969**, *26*, 310-343.
- (16) Chandra, S.; Chabot, J. F.; Morrison, G. H.; Leopold, A. C. *Science* **1982**, *216*, 1221-1223.
- (17) Cheney, K. B.; Pitkin, E. T. *J. Appl. Phys.* **1965**, *36*, 3542-3544.
- (18) Castaing, Raymond; Slodzian, Georges. *J. Microsc.* **1962**, *1*, 395-410.
- (19) Morrison, G. H. In "Secondary Ion Mass Spectrometry, SIMS III"; Benninghoven, A., et al. Eds.; Springer-Verlag: New York, 1982; pp 244-256.

RECEIVED for review June 7, 1982. Accepted August 25, 1982. Funding for this project was provided by the National Institutes of Health, the National Science Foundation, and the Office of Naval Research.